Article

De novo design of miniprotein antagonists of cytokine storm inducers

Buwei Huang[1,2,3,11], Brian Coventry[1,2,4,11], Marta T. Borowska[5,11], Dimitrios C. Arhontoulis[6,11], Marc Exposit[1,2,11], Mohamad Abedi[1,2], Kevin M. Jude[5,7], Samer F. Halabiya[2], Aza Allen[2], Cami Cordray[2], Inna Goreshnik[1,2,4], Maggie Ahlrichs[2], Sidney Chan[2], Hillary Tunggal[8], Michelle DeWitt[2], Nathaniel Hyams[9], Lauren Carter[2], Lance Stewart[2], Deborah H. Fuller[8], Ying Mei[6,9], K. Christopher Garcia[5,7,10] & David Baker[1,3,5] ✉

Cytokine release syndrome (CRS), commonly known as cytokine storm, is an acute systemic inflammatory response that is a significant global health threat. Interleukin-6 (IL-6) and interleukin-1 (IL-1) are key pro-inflammatory cytokines involved in CRS and are hence critical therapeutic targets. Current antagonists, such as tocilizumab and anakinra, target IL-6R/IL-1R but have limitations due to their long half-life and systemic anti-inflammatory effects, making them less suitable for acute or localized treatments. Here we present the de novo design of small protein antagonists that prevent IL-1 and IL-6 from interacting with their receptors to activate signaling. The designed proteins bind to the IL-6R, GP130 (an IL-6 co-receptor), and IL-1R1 receptor subunits with binding affinities in the picomolar to low-nanomolar range. X-ray crystallography studies reveal that the structures of these antagonists closely match their computational design models. In a human cardiac organoid disease model, the IL-1R antagonists demonstrated protective effects against inflammation and cardiac damage induced by IL-1β. These minibinders show promise for administration via subcutaneous injection or intranasal/inhaled routes to mitigate acute cytokine storm effects.

Cytokine release syndrome (CRS) is an acute systemic inflammatory syndrome involving the overproduction of proinflammatory cytokines and remains a global health threat[1]. CRS can be triggered by various diseases and therapeutic interventions including autoimmune diseases, CAR-T therapy, and antibody treatment, and also prompted by viral infections as occurred during the outbreak of SARS-COV-2, influenza, and MERS infections[2,3]. IL-6 and IL-1β are potent pro-inflammatory cytokines controlling both the adaptive and innate immune response[4] (Fig. 1a), but in the CRS context, the overproduction of IL-6 and IL-1β can cause devastating effects by excessively activating immune cells and reinforcing the cytokine production cycle[5–7], leading to severe tissue damage and injury.

[1]Department of Biochemistry, University of Washington, Seattle, WA, USA. [2]Institute for Protein Design, University of Washington, Seattle, WA, USA. [3]Department of Bioengineering, University of Washington, Seattle, WA, USA. [4]Howard Hughes Medical Institute, University of Washington, Seattle, WA, USA. [5]Department of Molecular and Cellular Physiology, Stanford University School of Medicine, Stanford, CA, USA. [6]Molecular and Cellular Biology and Pathobiology Program, Medical University of South Carolina, Charleston, SC, USA. [7]Howard Hughes Medical Institute, Stanford University School of Medicine, Stanford, CA, USA. [8]Department of Microbiology, University of Washington, Seattle, WA, USA. [9]Department of Bioengineering, Clemson University, Charleston, SC, USA. [10]Department of Structural Biology, Stanford University School of Medicine, Stanford, CA, USA. [11]These authors contributed equally: Buwei Huang, Brian Coventry, Marta T. Borowska, Dimitrios C. Arhontoulis, Marc Exposit. ✉e-mail: dabaker@uw.edu
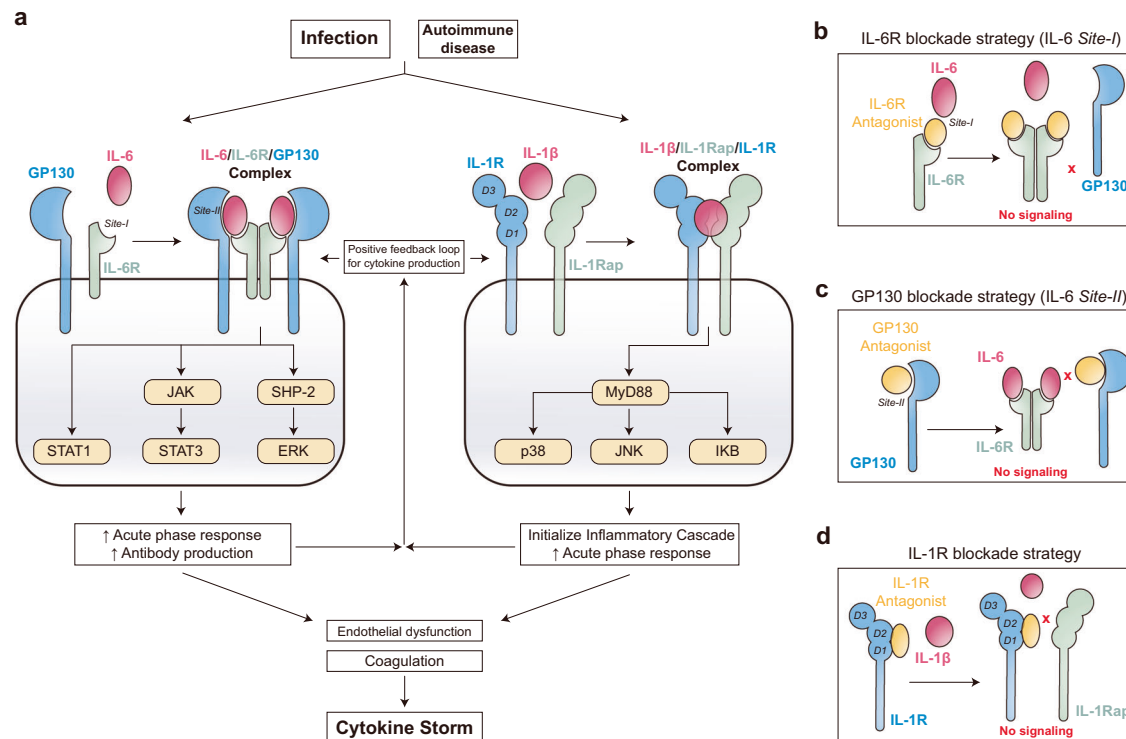
Fig. 1 | IL-6 and IL-1 in cytokine and antagonist design strategy. a Signaling pathway of IL-6 and IL-1 in cytokine storm. **b** IL-6R blockade design strategy by directly competing IL-6 binding to IL-6R at site-I[16]. **c** GP130 blockade design strategy by interfering with the IL-6/IL-6R complex binding to GP130 at site-II[16]. **d** IL-1R blockade design strategy by directly competing IL-1b binding to IL-1R at the intersection of domain1 (D1) and doamin2 (D2)[19].

During serious viral infection in the lung, elevated levels of IL-6 and IL-1β result in overactivation and excessive recruitment of neutrophils and macrophages, damaging the alveolar epithelial cells, which can cause tissue injury and respiratory failure associated with acute respiratory distress syndrome (ARDS)[8]. Antagonists of IL-6 and IL-1β signaling have been broadly used to treat long-term systematic autoimmune diseases such as rheumatoid arthritis (RA), but it is unclear whether systematic inhibition of IL-6 and IL-1β signaling will benefit patients with acute CRS due to viral infection or therapeutic interventions. Neither the IL-6R inhibitor Tocilizumab nor the IL-1R inhibitor Anakinra significantly improved the survival of critical SARS-COV-2 patients[9–12]. Administering long-circulating immunomodulation drugs to severe or critical patients also can increase the risk of pathogen infection[10,11]. Therefore, alternative therapeutic strategies that provide local and short-term immunomodulation in the lung to deal with acute ARDS while avoiding longer-term immune suppression are needed[10,13].

De novo protein design has been used to generate small protein inhibitors (minibinders) that bind to their targets with high affinity, have high thermostability enabling local administration, and have short circulation times due to filtration in the kidney[14]. Examples include minibinders that efficiently block the SARS-CoV-2 receptor binding domain and protect animals from viral infection when introduced via intranasal delivery[15], and that inhibit signaling through the IL-7 cytokine receptor[14]. We reasoned that de novo-designed minibinders to the ligand binding sites of the IL-6 receptor and the IL-1 receptor would result in effective antagonists against viral-induced CRS that could be compatible with intranasal/inhaled application for short-term immunomodulation.

In this work, we show the computational design and characterization of potent antagonists against three cytokine receptors (IL-6R, GP130, and IL-1R1) that play a key role in the progression of cytokine storms.

Results

Design of cytokine receptor antagonists

IL-6 signals by bringing together the IL6-specific IL-6R receptor subunit with the shared GP130 receptor subunit into a higher-order complex[16], while IL-1 signals by bringing together the IL-1R subunit with IL-1R accessory protein[17]. To computationally design antagonists that block the signaling of IL-6, we selected the IL-6 binding site on IL-6R (PDB 1N26[18]) to interfere with the IL-6 binding via Site-I (Fig. 1b), and IL-6 binding site on GP130 (PDB 1P9M[16]) to interfere with IL-6 binding at Site-II (Fig. 1c). To develop antagonists to block IL-1b signaling, we chose the ligand binding site on the hinge region between domain1 and domain2 in IL-1R (PDB 1IRA[19]) (Fig. 1d).

For each of these target regions, we used Rosetta to design small protein binders. First, several hydrophobic residues overlapping the native ligand binding site were selected, and a rotamer interaction field (RIF) was generated around these residues with the RIF docking software[20]. A miniprotein scaffold library was then rigidly docked to the selected target residues using Patchdock[21], followed by a local search to optimize sidechain-sidechain interactions using Rifdock[14]. The sequence and the structure of the initial docks were optimized with RosettaFastdesign[14] followed by one round of diversification through RosettaMotifgraft[22] and further optimization with RosettaFastdesign. The combined output designs from both rounds were further filtered with Rosetta metrics including ddg, contact_patch, ss_sc, worst9mer, mismatch_prob, contact_molecular_surface, and sap score[14]. For each target, the top 100,000 candidates passing all Rosetta filters were chosen as the final pool for experimental screening.

Experimental screening and characterization of the designed minibinders

The designed proteins are 65 amino acids or less, and hence can be encoded on single long oligonucleotides on low-cost oligonucleotide arrays. Oligonucleotides encoding the amino acid sequences were
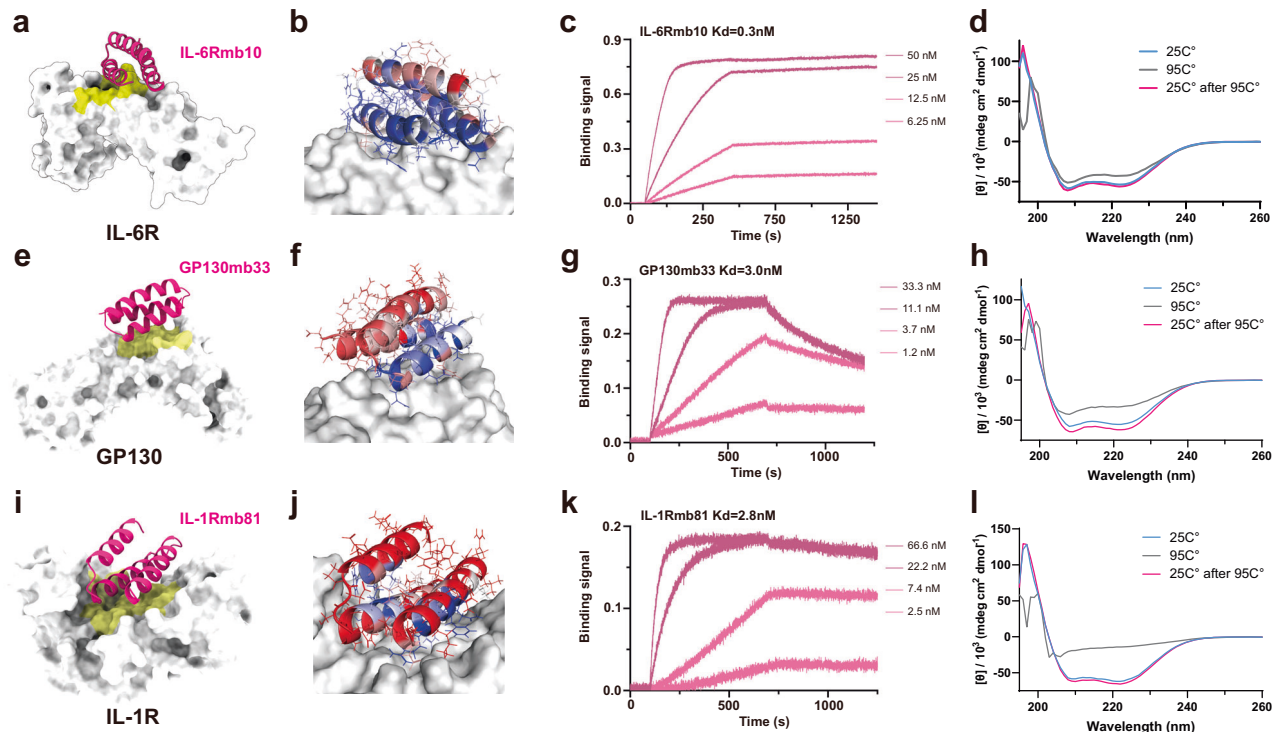
Fig. 2 | Designed minibinder antagonists and characterization. a, e, and i Design model of minibinder in complex with targets. a IL-6R (PDB: 1P9M, 1N26); e GP130 (PDB: 1P9M); i IL-1R (PDB: 1IRA). The major binding sites/hotspots were colored yellow. b, f, and j The zoomed interface of the initial IL-6R minibinder design model colored by conservation calculated based on site mutagenesis screening. The designed minibinders are colored based on entropy, where blue indicates the conserved position and red indicates the less conserved position. c, g, and k Binding affinity measurement using BLI. 50 nM biotinylated targets were captured on SA-tips and incubated with given concentrations of minibinders. Binding affinities were estimated using the Octet ForteBio software. d, h, and l CD spectra before and after melting. Source data are provided as a Source Data file (raw data for c, g, and k are provided in the raw data file zenodo.org (accession code: 12797779) due to file size).

transformed into yeast and screened against the corresponding target protein using yeast surface display using fluorescence-activated cell sorting (FACS) followed by next-generation sequencing (NGS)[14,23] (Supplementary Fig. 5). The enrichment for each minibinder was calculated and the binding affinity KD was estimated based on the relative enrichment at different target concentrations. We set a threshold of KD < 10 uM measured in this way as a successful hit and identified 1016 initial hits for IL-6R, 914 initial hits for GP130, and 216 initial hits for IL-1R.

We sought to optimize the binding affinity and validate the binding mode for the top 50 initial hits for each target with an additional round of site saturation mutagenesis (SSM) library selection, where each residue in a designed binder was mutated to each of the other 19 amino acids one at a time. After sorting the new SSM libraries against the corresponding target using FACS and NGS, we estimated the KD and calculated the relative enrichment for each single mutant over the KD of its parent sequence. We selected designs with SSM maps (Supplementary Fig. 11) consistent with the computational design model (conservation at the designed binding site and in the protein core) and further optimized their affinity with another round of combinatorial library (combining the most enriched substitutions in the SSM) screening using FACS followed by NGS (Supplementary Fig. 5).

We expressed the optimized designs for each target in E. coli and purified the proteins using immobilized metal chelate chromatography followed by size exclusion chromatography (SEC) (Supplementary Fig. 6a, c, and e). The binding affinities of the purified minibinders were estimated by biolayer interferometry (BLI) against the biotinylated target protein (Supplementary Fig. 6b, d, and f). The top candidate for IL-6R (IL-6Rmb10) bound IL-6R at 300 pM KD (Fig. 2c); the best binding affinity binder for GP130 (GP130mb33)

bound GP130 at 3.0 nM KD (Fig. 2g); and IL-1Rmb81 bound to IL-1R1 at 2.8 nM (Fig. 2k). The designs are quite specific; no binding was observed to related receptors in the same family (IL-27R and IL-11R for IL-6Rmb10, IL-36R for IL-1Rmb81), indicating specific binding (Supplementary Fig. 8). Circular dichroism (CD) temperature melting studies showed that IL-6Rmb10 and GP130mb33 had melting temperatures greater than 95 °C with nearly identical spectra at 25 °C and 95 °C (Fig. 2d, h and Supplementary Fig. 12a, b), and no cooperative unfolding transition (Supplementary Fig. 12d, e; there is a monotonic decrease in mean residue ellipticity arising from temperature dependent native state CD signal as observed for many other proteins), while IL-1Rmb81 had a melting temperature of 76.1 °C (Fig. 2l and Supplementary Fig. 12c, f). For all three proteins, the spectra at 25 °C before and after incubation at 95 °C were nearly identical, indicating robustness to high-temperature exposure.

Minibinders function as potent antagonists

Next, we investigated the capability of the designed binder to inhibit the signaling of the corresponding cytokines. For the IL-6 pathway, we monitored phosphorylation of the downstram transcription factor STAT3 using a phosphoflow assay. IL-6Rmb10 was a potent IL-6 competitor in human THP-1 cells: 100 nM of IL-6Rmb10 increased the EC50 for STAT3 activation by IL-6 from 0.3 nM in the absence of inhibitor to 21.7 nM, a 74.7 fold increase (Fig. 3a and Supplementary Table 3). The designed GP130 inhibitor GP130mb33 increased the EC50 of IL-6 STAT3 activation by only 3-fold (from 0.3 nM to 0.8 nM), (Fig. 3a and Supplementary Table 3), but decreased Emax by nearly 40%. The very different modes of antagonism of the IL-6R and GP-130 binders are consistent with the overall design strategy (Fig. 1b, c). The IL-6R inhibitors directly competed out the binding of IL-6 to the IL-6R, shifting the dose-response curve (altering EC50) without impacting the Emax.
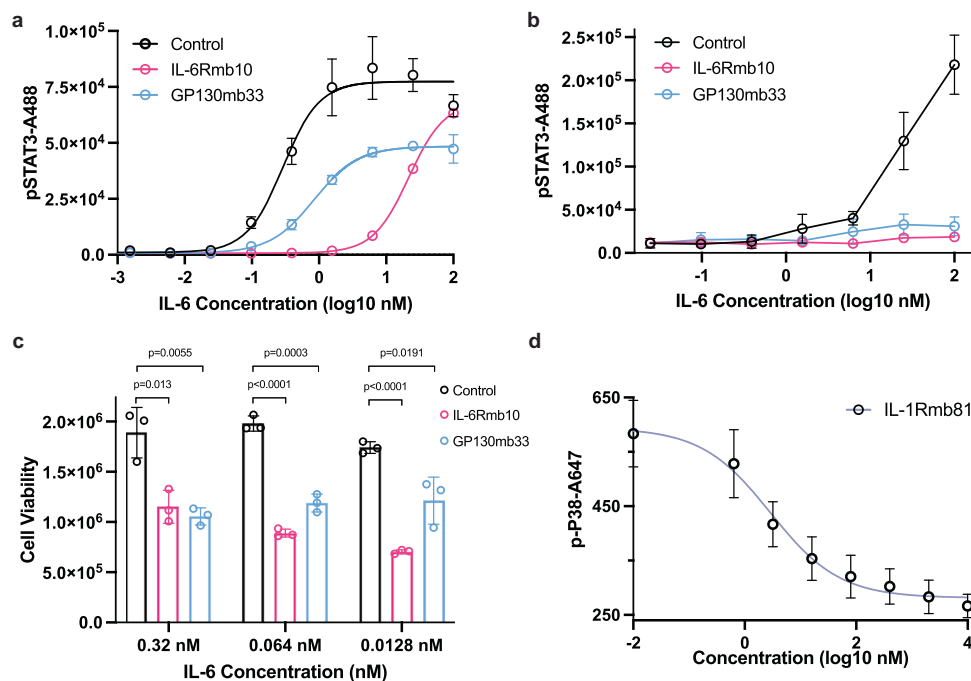
Fig. 3 | Cytokine signaling inhibition effects of designed antagonists. a, b Measurement of antagonism of STAT3 signaling by the IL-6R and GP130 antagonists using phosphoflow. THP-1 cells (a) or HUVEC cells (b), which do not express IL-6R, were titrated with increasing concentrations of IL-6 alone or with 100 nM IL-6Rmb10 or GP130mb33 (a) or preincubated with 200 nM soluble IL-6R for trans-signaling followed by addition of IL-6 alone or with 500 nM IL-6Rmb10 or GP130mb33 (b). c Antagonism of IL-6 induced proliferation. Starved TF-1 cells were incubated alone or with 1 uM of IL-6Rmb10 or GP130mb33 and stimulated with three different concentrations of IL-6 for 2 days before assessing cell viability. The P value is calculated by an unpaired two-tailed t-test. d Measurement of antagonism of P38 signaling by IL-1R antagonism measured by phosphoflow. THP-1 cells were titrated with increased concentrations of IL-1Rmb81 in the presence of 10 nM IL-1b. For a–d, the mean values were calculated based on biological replicates with sample size $n = 3$ and error bars represent SEM. The IC50s were measured by non-lin fit using GraphPad Prism 8.0.2. Source data is provided as a Source Data file.

Conversely, the GP130 antagonists do not block IL-6 binding to IL-6R and hence had only small effects on the EC50; instead, they disrupt subsequent recruitment of the GP130 signaling domain, reducing overall STAT3 activation and hence Emax.

IL-6 can induce *trans*-signaling, where IL-6 bound to a soluble form of the IL-6 receptor (sIL-6R) is recruited to GP130 on the cell surface, enabling IL-6 signaling in cells that do not express the full-length membrane-bound IL-6R, thus broadening the scope and impact of IL-6 activity within the body[24]. To evaluate the capacity of our designed antagonists to block this non-canonical pathway, we conducted IL-6 trans-signaling assays in human umbilical vein endothelial cells (HUVEC) that lacked the expression of IL-6R but still expressed GP130. IL-6 treatment induced potent phosphorylation of STAT3 which was effectively blocked by both IL-6Rmb10 and GP130mb33 (Fig. 3b and Supplementary Fig. 7). Thus both IL-6Rmb10 and GP130mb33 can inhibit both cis and *trans* IL-6 signaling pathways.

IL-6 signaling was also reported to trigger the cellular proliferation of bone marrow cells[25]. To assess the efficacy of our designed antagonists in inhibiting IL-6 signaling, we conducted a cell proliferation assay using TF-1 cells. The cells were treated with IL-6 alone or in combination with either 1 uM IL-6Rmb10 or GP130mb33. After 48 h incubation, both antagonists significantly reduced IL-6-induced proliferation of TF-1 cells (Fig. 3c).

We next evaluated the IL-1 inhibition of the IL-1R antagonists by quantifying the phosphorylation of P38, a component of the IL-1-activated MAPK signaling cascade. The high-affinity candidate IL-1Rmb81 strongly reduced the activation of phosphorylated P38 in THP-1 cells triggered by 10 nM of IL-1b, with an IC50 of 2.8 nM close to the Kd of IL-1mb81 for IL-1R1 (Fig. 3d).

Structure determination

We were able to solve the crystal structure of GP130mb33 in complex with GP130. In the crystal structure, the design binds to GP130 almost exactly as in the computational design model: when the crystal structure and design model are aligned on the GP130 receptor, the Ca mean square deviation over the monomers between the design model and crystal structures is 1.03 A (Fig. 4a). The major binding residues close to the interface have nearly identical side-chain configurations in the crystal structure and the design model (Fig. 4a). We also obtained the structure of GP130 in complex with GP130mb44, a variant of GP130mb33, which again was very close to the computational design model (Supplementary Fig. 9). We were able to solve the monomer structure of IL-6Rmb6 (Fig. 4b) and IL-1Rmb80 (Fig. 4c) which were also nearly identical to the computational design models (RMSD = 0.93 A and 0.53 A, respectively). These results indicate the very high accuracy of our computational design approach.

Designed antagonists reduced damage in human cardiac organoids (hCOs)

We investigated the inhibition function of the IL-1R antagonists in a hCOs model. Previous studies have shown that IL-1b can induce inflammation in hCOs that mirrors the cytokine storm caused by SARS-COV-2 infection: the cardiac organoids have reduced cardiac function and exhibit pathological cardiac fibrosis after IL-1b stimulation[26]. In this model (Fig. 5a), both IL-1Rmb80 and IL-1Rmb81 reduced the cardiac damage and fibrosis caused by the IL-1b stimulation, indicated by recovered fractional area change (FAC) compared to IL-1b treatment alone (Fig. 5b). IL-1Rmb treatment also led to recovery of the morphologies of the hCOs compared to the IL-1b alone group (Fig. 5c, d).
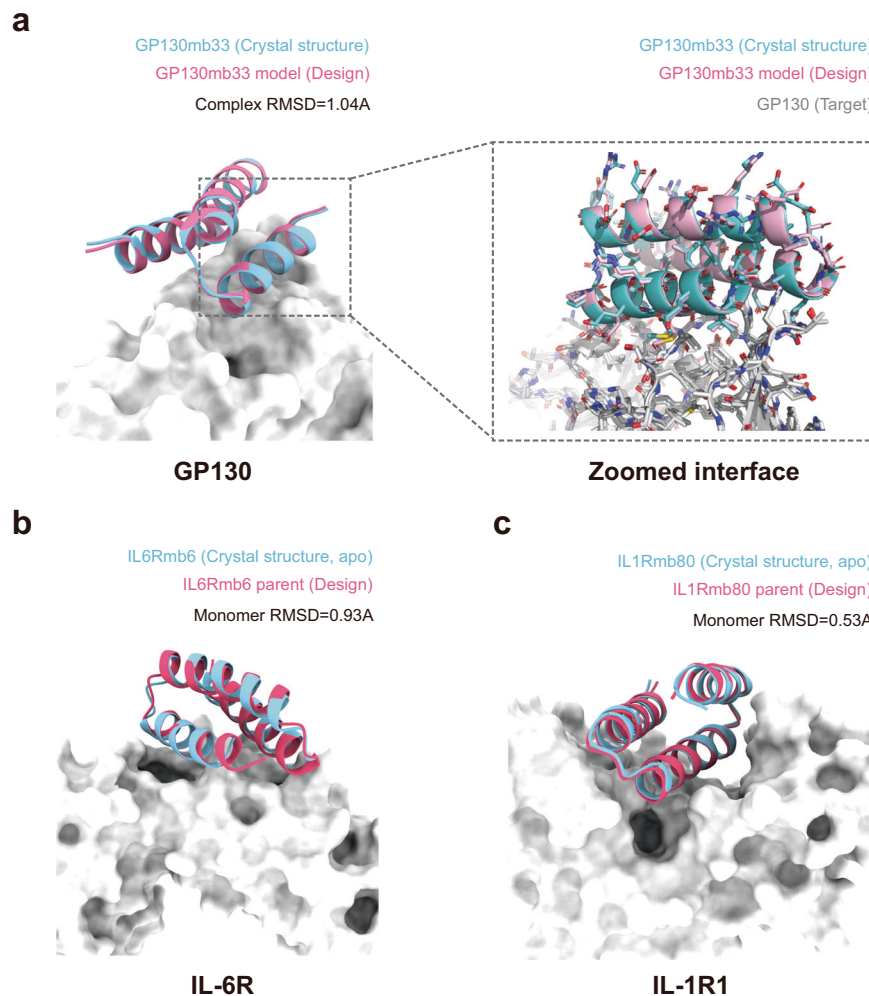
a
GP130mb33 (Crystal structure)
GP130mb33 model (Design)
Complex RMSD=1.04A

GP130mb33 (Crystal structure)
GP130mb33 model (Design)
GP130 (Target)

GP130

Zoomed interface

b
IL6Rmb6 (Crystal structure, apo)
IL6Rmb6 parent (Design)
Monomer RMSD=0.93A

IL-6R

c
IL1Rmb80 (Crystal structure, apo)
IL1Rmb80 parent (Design)
Monomer RMSD=0.53A

IL-1R1

Fig. 4 | Crystal structures of designed antagonists. a Left, alignment of design model of GP130mb_original (before optimization) in complex with GP130 on the experimentally determined crystal structure of the GP130/GP130mb33 complex. The aligned complex rmsd using pymol2 is indicated. Right, zoom in on the interface of the aligned complex model. **b**, **c** Superimpositions of the experimentally solved monomer structures of designed antagonists on the design models (before optimization); the targets are shown as gray surfaces. The aligned monomer rmsds using pymol2 are indicated. **b** IL-6Rmb6 structure aligned to IL-6Rmb_original in complex with IL-6R (design model). **c** IL-1Rmb80 structure aligned to IL-1Rmb_original in complex with IL-1R (design model).

We next examined the cytokine profiles in the organoids. IL-1b stimulation significantly elevated the pro-inflammatory cytokine levels including Interferon γ, IL-6, IL-8, and IL-10, while treatment with IL-1Rmb80 and IL-1Rmb81 reduced the levels of these cytokines back to normal levels (Fig. 5e). In contrast, inhibition was not observed by our designed IL-6R and GP130 antagonists (Fig. 5e), consistent with the previous finding that FDA-approved Tocilizu-mab does not show efficacy in the same organoid model[26], sug-gesting a limitation of this model in recapitulating IL-6 activation (Supplementary Fig. 4). The potent antagonism of IL-1b induced inflammation in the organoid model suggests that the designs could have considerable potential in calming down the cytokine storm caused by SARS-COV-2 and other viral and environmental triggers.

Discussion
Our results highlight the power of computational protein design to create antagonists for therapeutic cell surface receptor targets. The high binding affinities, the potent neutralization of Stat signaling, and the close agreement between the crystal structures and computational design models highlight the control now afforded by computational design methodology.

The antagonists described here have considerable potential for the treatment of cytokine storm—they potently block the IL-1 and IL-6 signaling, and their high stability and ready manufacturability should be considerable advantages. The circulation time of mini-proteins is much less than antibodies due to filtration in the kidney, and some half-life extension by pegylation, lipidation, or albumin binder fusion may be necessary, but unlike the treatment of chronic disease, the treatment of acute responses like cytokine storm could benefit from shorter half-life antagonists as high doses could be administered to completely block short term responses without risk of longer-term negative effects from immunosuppression. In vivo characterization of the designed antagonists in cytokine storm and other models, and characterization of their immunogenicity and serum stability, are important next steps towards therapeutic deployment.

Methods
Computational binder design
The minibinders against IL-6R, GP130, and IL-1R1 were computationally designed via a Rosetta-based binder design approach[14]. Briefly, the structures of IL-6R, GP130 (PDB 1P9M), and IL-1R1 (PDB 1IRA) were coordinate-refined using Rosetta Fastrelax. The residues in the hydrophobic patches near the cytokine binding sites were selected as
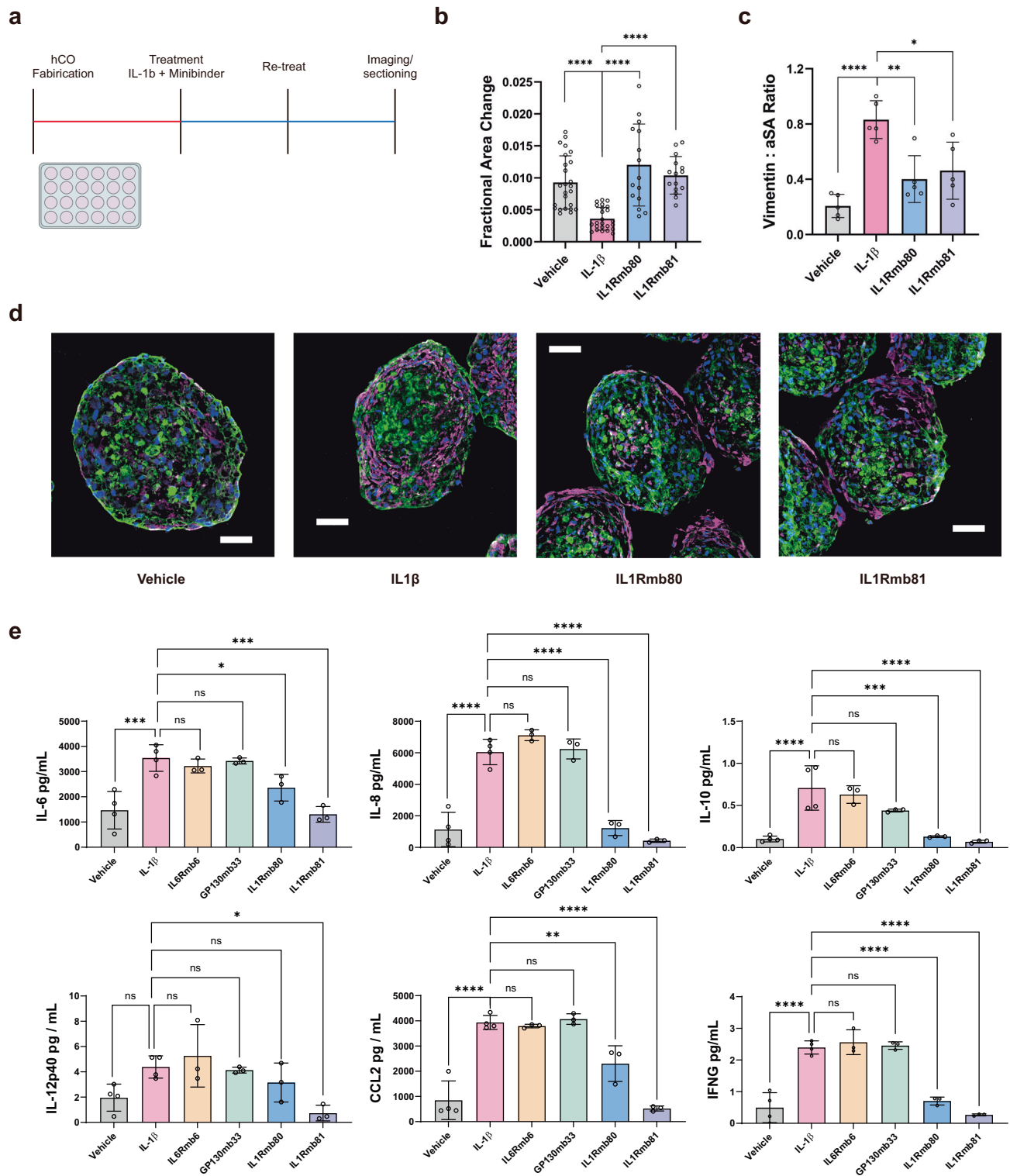
Fig. 5 | Functional study of designed antagonists in the human organoid model.
a Treatment regimen for injured hCOs. **b** FAC quantification. Error bars are from
$n = 16$ biological replicates. **c** Calculated ratio of Vimentin vs α-SA in the immu-
nofluorescent staining assay. The error bar is shown with biological replicate $n = 5$.
d Immunofluorescent staining of hCOs or IL-1β stimulated hCOs on Day 4
(green = α-SA, red = Vimentin, and blue = DAPI). The scale bar represents 50 μm for
each image. **e** Cytokine multiplex comparison among IL-1R inhibitors, IL-6Rmb6,

and GP130mb33 inhibitors. Results were represented as fold change of cytokines in
the Day 4 supernatant as compared to hCOs. The error bar is shown with biological
replicate $n = 4$. For **b**, **c**, and **e** data were presented as mean values +/− SEM, and
P values were calculated via an ordinary one-way ANOVA test. For P values, ns
represents $P > 0.05$, *represents $P < 0.05$, **represents $P < 0.01$, ***represents
$P < 0.001$ and ****represents $P < 0.0001$. Source data are provided as a Source
Data file.

hotspot residues. A pre-designed de novo protein scaffolds including 40 k various topologies were docked against the hotspot residues via Patchdock followed by Rifdock protocol. Twenty million rifdock outputs were collected and ran into a fast-round sequence design and side-chain minimization scored by Rosetta Predictor to report ddg, contact_molecule_surface, and contact_patch values. The top 2.5 million backbones were selected for a full sequence design run using two rounds of Rosetta Fastdesign followed by one round of Rosetta Fast relax based on the Rosetta beta_nov16 score function. After filtering with interface metrics (see below for detailed filter values) including ddg, contact_molecular_surface, contact_patch, and monomer metrics including worst9mer, ss_sc, mismatch_prob, the top candidates were then resampled with Rosetta Motifgraft and FastDesign. Candidates passing previous filters were then filtered again with exposed hydrophobicity (termed sap_score[14]) and optimized with a net charge of −7. Then the sequences of the best 100,000 designs were padded to 65AA with G/S sequences, and the padded sequences were reverse-translated to DNA with codon optimization. The DNA oligo encoding the top 100,000 designs for each target was ordered for experimental binding screening in yeast display. All the script and option flag files used to generate the designs will be provided in a public server before publication.

In-silico filter metrics[14,22,27]:

```
ddg < -40

Contact_molecule_surface > 400
Contact_patch > 150

worst9mer < 0.4

worst9mer_helix < 0.15

score_per_res < -2.4

ss_sc > 0.8
mismatch_prob < 0.07
```

Detailed hotspot residue selection:
IL-6R (PDB 1N26/1P9M_C):

```
Patchdock residues: 11,92,129,130,154,179
Rifdock residues: 11,63,64,92,127,128,129,130,131,154,
177,178,179,180,181,197
```

GP130 (PDB 1P9M_A):

```
Patchdock residues: 42,47,64,67,68,69,70,95,130
Rifdock residues: 42,43,44,45,47,64,65,66,67,68,69,70,
71,93,95,96,130,131
```

IL-1R (PDB 1IRA_B):

```
Patchdock residues: 8,21,106,119,121,122,125
Rifdock residues: 6,8,10,20,21,22,23,106,108,119,120,
121,122,124,125,157
```

Target protein preparation

Baculoviruses of human GP130, and IL-1R ECDs were prepared by transfecting and amplifying into Sf9 cells. Viruses were further used to infect Hi5 cells and grown in the presence of 5 μM kifunensine. After approximately 72 h, secreted proteins were purified from the supernatant by passing over a Ni-NTA agarose column and eluted with 200 mM imidazole in HBS buffer (10 mM HEPES pH 7.4, 150 mM NaCl). Eluted samples were treated 1:75 (*w/w*) with EndoHf (NEB), and 1:100 (*w/w*) with carboxypeptidases A and B (Sigma) to remove purification tags and then incubated overnight at 4 °C. Samples were further combined with a 1.5-fold molar excess of GP130mb or IL-6Rmb purified separately and exchanged by FPLC using a Superdex 75 10/300 GL column (Cytiva) into HBS buffer. Peak fractions were inspected by SDS-PAGE, pooled, and concentrated to 15 mg/ml.

Yeast surface display and NGS

The DNA oligo encoding the designed protein was transformed into an EBY-100 yeast strain with high-efficiency electroporation[14,27]. After growing the transformed yeast in C-Trp-Ura medium for 2 days at 30 °C, the yeast cells were centrifuged at 5000 g for 2 min and were buffer exchanged to SGCAA buffer at 10^7 cells/ml density. After incubation in SGCAA buffer overnight, the induced cells displayed the designed protein on their surface and went through first-round expression sorting. The yeasts were stained with anti-c-Myc fluorescein isothiocyanate (FITC, Miltenyi Biotech, 1:100) for 30 min followed by two rounds of wash with PBSF (PBS + 0.75% BSA). The labeled yeasts were then sorted for expression level in FACS and the cells with high FITC levels were collected and further enriched in CTUG buffer for 2 days followed by 1 day induction in SGCAA buffer. The grown cells were then incubated with the corresponding biotinylated target protein (IL-6R, GP130, or IL-1R) and stained with streptavidin–phycoerythrin (SAPE, ThermoFisher, 6.8:100) and anti-c-Myc FITC (1:100) followed by PBSF wash and FACS. The PE/FITC double positive cells were further enriched with another round of sorting and another round of titration series with target concentrations ranging from 1 nM to 1000 nM. After three rounds of binding enrichment, the individually collected yeasts at each round were lysed followed by DNA amplification and NGS. The NGS data were then processed and estimated binding affinity was predicted by a statistic fitting model[27]. We observed 1016 successful hits for IL-6R, 914 successful hits for GP130, and 216 hits for IL-1R1 (successful hits were determined by estimated KD < 10 uM).

Protein expression and purification

DNA fragments (IDT Gblock) encoding the designed miniprotein sequences were cloned into the pET29 vector (GenScript, N-terminal 6-His tag) by Gibson assembly. The cloned vectors were then transformed into BL21 (DE3) Competent E. coli strain (C2527H) with 45 s heat shock followed by 1 h growth in SOC media. The transformed E coli were then inoculated in 50 ml of autoinduction medium (20 g/l Terrific Broth + 20 mM MgSO4 + 1:50 5052 buffer (25% glycerol, 2.5% glucose, and 10% α-lactose)[28]) with 50 ug/ml of kanamycin and grown for 24 h at 37 °C. On day 2, the E coli were centrifuged at 5000 g for 30 min, buffer exchanged to 40 ml of 30 mM Tris-HCL (pH 8.0), and were lysed with a sonicator for 5 min. After centrifuging at 15,000 g for 30 min, the supernatant of the lysates was flowed through a gravity column with Ni-NTA resin (Qiagen), followed by two rounds of washing with wash buffer (TBS + 20 mM imidazole) and elution with elution buffer (300 mM NaCl, 30 mM Tris-HCL (pH 8.0) + 400 mM imidazole). The eluted proteins were then purified with SEC (GE Healthcare Akta with Superdex 75 10/300 GL column). The fractions were collected and combined based on the main monomeric fractions in SEC. Protein concentrations were determined by Nanodrop at UV 280 nm and were normalized by extinction coefficient.

CD

The CD characterization was conducted using the JASCO-1500 instrument. Purified miniproteins at 0.2 mg/ml concentration in PBS were loaded into the transparent 1 mm glass cuvette and wavelength scan was sequentially scanned at 25 °C, 95 °C, and 25 °C right after heating to 95 °C. The Tm curves were obtained by recording the ellipticity value at 220 nm at increased temperature from 25 °C to 95 °C at 1 °C intervals. The Tm values were measured by calculating the

inflection point of the sigmoidal fitted curve using GraphPad Prism software.

Binding affinity measurements

The binding affinity for the minibinder antagonists was measured using Octet RED96 (ForteBio). Streptavidin-coated biosensors (ForteBio) were loaded with biotinylated target proteins at 50 nM final concentration in Octet buffer (10 mM HEPES, 150 mM NaCl, 3 mM EDTA, 0.05% surfactant P20 and 1% BSA) for 5 min, washed with buffer for 5 min, associated with titrated concentrations of the corresponding miniproteins for 8 min for Kon measurement, and dipped back in buffer for Koff measurement. Due to the massive size difference between the biotinylated GP130 and IL-1R1, a Maltose binding protein fusion with the corresponding designed binder was used in BLI. The binding affinity (Kd) was determined with the octet analysis software.

Surface plasmon resonance (SPR)

Crossreactive binding of IL-6Rmb10 and IL-1Rmb81 to their original receptors (Fc tagged IL-6R and IL-1R1) and homologous receptors (Fc tagged IL-27R, IL-11R, and IL-36R) were measured in Biacore 8 K using a Protein A chip (Cytiva #29127556) at 5 μg/ml target concentration. The binding traces were collected by running single-cycle kinetics at increased binder concentration (six series with 8-fold titration starting at 1000 nM). The binders and targets were diluted in HEPES buffer (Cytiva #BR100669).

Structure determination of unbound IL-1Rmb

IL-1R Domain 1 and Domain 2 (IL-1R D1D2) were mixed with a 1.5-fold molar excess of IL-1Rmb, and the proteins were copurified over an S75 Increase column (Cytiva). Peak fractions were inspected by SDS-PAGE, pooled, and concentrated to 23 mg/ml. Crystallization trials were performed at 23 mg/ml and 12 mg/ml, and crystals were obtained from the JCSG + screen (molecular dimensions) at 12 mg/ml from a precipitant solution containing 0.17 M ammonium sulfate, 25.5% polyethylene glycol 4000, and 15% glycerol. Crystals were cryoprotected with the addition of 15% ethylene glycol and flash-cooled in liquid nitrogen. Diffraction data were collected at the Stanford Synchrotron Radiation Laboratory (SSRL) beamline 12-1. Reflections were indexed, integrated, and scaled using XDS[29] in space group C2 with unit cell dimensions $a = 83.34$ Å, $b = 55.22$ Å, $c = 53.88$ Å, and $b = 103.54°$. The structure was solved using Phaser[30] using the predicted model of IL-1Rmb80 as a search model, revealing four copies of IL-1Rmb80 in the asymmetric unit and no IL-1R D1D2, with a calculated solvent content of 37%. The structure was refined with iterative cycles of interactive refinement in Coot[31] and reciprocal space refinement in PHENIX[32], including TLS, individual B-factor, and occupancy refinement. The final structure has 100% of residues in the favored regions of the Ramachandran plot. Data collection and processing statistics are listed in (Supplementary Table 1). A representative density map of the structure is provided in Supplementary Fig. 10c.

Structure determination of unbound IL-6Rmb

IL-6R + IL-6Rmb6 complex was set up for crystallization at room temperature by sitting drop vapor diffusion. However, we obtained only crystals of IL-6Rmb6 alone in multiple conditions. The final structure was solved from crystals obtained in JCSG + E1 condition (1 M Trisodium citrate, 0.1 M Sodium cacodylate pH 6.5), harvested, and flash frozen with 3.3 M sodium malonate pH 6.5 as cryoprotection at 15 mg/ml concentration. Crystals diffracted to 1.48 Å resolution at the SSRL beamline 12-1. The data were processed, scaled, and merged using iMosflm[33], truncated with ccp4, and a search model using PHASER[30] as a molecular replacement tool was done with PHENIX[32] 29 Cycles of manual model building, and refinement (torsional non-crystallographic symmetry restraints applied throughout) were done with COOT and PHENIX[31,32]. Data collection and processing statistics

are listed (Supplementary Table 1). A representative density map of the structure is provided in Supplementary Fig. 10a.

Structure determination of GP130mb in complex with GP130

Crystals of complexes were grown at room temperature by sitting drop vapor diffusion. Crystals for GP130 + GP130mb33 and GP130 + GP130mb44 were obtained in JCSG + D12 condition (0.04 M potassium phosphate monobasic, 16% polyethylene glycol 8000, 20% glycerol) at 15 mg/ml concentration. All crystals were harvested, and flash frozen directly from the drop and without cryoprotection. Crystals diffracted to 3.3 Å resolution for the GP130 + GP130mb33 complex and 1.87 Å resolution for the GP130 + GP130mb44 complex at the advanced photon source beamline 23IDD. The data were processed, scaled, and merged using iMosflm[33], truncated with ccp4, and a search model using PHASER[30] as a molecular replacement tool was done with PHENIX[32] Cycles of manual model building, and refinement (torsional non-crystallographic symmetry restraints applied throughout) were done with COOT[31] and PHENIX[32]. Data collection and processing statistics are listed in (Supplementary Table 1). A representative density map of the structure is provided in Supplementary Fig. 10b.

Phospho-STAT3 for IL-6 signaling inhibition

For STAT signaling, THP-1 human monocyte cell line cells were grown in RPMI complete media (corning), then 100k cells/well were incubated with 100 nM antagonist (GP130mb33, IL-6Rmb10, or none) for 10 min @ 37 °C (no wash), then stimulated with hIL-6 (0.01 pM–100 nM, PeproTech) for 30 min @37 °C prior to fixation with 4.25% formaldehyde (BD Cytofix™ Fixation Buffer) for 10 min at 37 °C. Cells were pelleted and re-suspended in 87.7% methanol (BD Phosflow™ Perm Buffer III). Cells were washed in Staining buffer (PBS with 2% FBS, BD Pharmingen™ Stain Buffer) and stained with antibodies against STAT3 pY705 Alexa Fluor® 488 Mouse Anti-Stat3 (BD Biosciences, 557814, pY705, 1:100 concentration) for 30 min at room temperature. The fluorescence intensity of pSTAT staining was analyzed using an Attune NxT flow cytometer. The gating strategy of the representative flow plot is provided in Supplementary Fig. 1. The Alternative method implemented by Supplementary Fig. 7 is provided in Supplementary Method 1.

IL-6 proliferation assay

TF-1 cells were starved overnight in RPMI medium with 10% FBS without GM-CSF supplementation. For the proliferation assay, 15k cells/well were incubated with either 1 uM of IL6Rmb10, 1 uM of GP130mb33, or media without antagonist for 10 min @ 37 °C (no wash), then stimulated with hIL-6 (PeproTech) at 12.8 pM, 64 pM, or 320 pM and cultured at 37 °C for two days. Cell viability was then assessed with a luminescence-based assay using CellTiter-Glo 2.0 (Promega G9241) according to the manufacturer's instructions.

Trans-complementation inhibition assay

HUVEC cells, which express GP130 but not IL-6R, were used to evaluate the antagonists in the context of IL6 trans-signaling with soluble IL-6R. HUVEC cells were incubated with 200 nM of soluble IL-6R (Acrobiosystems ILR-H4223) and either 500 nM of IL-6Rmb10, GP130mb33, or no antagonist for 10 min @ 37 C (no wash), then stimulated with hIL-6 (0.01 pM–100 nM, PeproTech) for 30 min @37 °C. Signaling through phosphorylated STAT3 was assessed using a phosphorylation flow assay as described above using Alexa Fluor® 488 Mouse Anti-Stat3 (BD Biosciences, 557814, pY705, 1:100 concentration). The gating strategy of the representative flow plot is provided in Supplementary Fig. 2.

Phospho-p38 MAPK for IL-1 signaling inhibition

THP-1 cells were seeded in a 96-well plate in DMEM medium with 10% FBS. The cells were then incubated with titrated concentrations of IL-1R inhibitors for 20 min, with the untreated group as negative control.

The cells were then stimulated with 10 nM IL-1b (ACROBiosystems, P01584-1). After 10 min stimulation at 37 °C, the cells were immediately fixed with 1:1 Cytofix buffer (BD Bioscience, 554655) at 37 °C for 10 min. After washing with cold stain buffer (BD Bioscience, BDB554656), the cells were permeabilized with Perm Buffer (BD Bioscience, 558050) for 30 min on ice. After washing twice with stain buffer, the cells were incubated with anti-phospho-P38-AF647 antibody (Cell Signaling, 4552 S, 1:100) at a 1:100 ratio for 30 min in the dark. The cells were then washed twice with stain buffer and ran through Flow Cytometry (Attune NxT). The gating strategy of the representative flow plot was provided in Supplementary Fig. 3.

Cell culture

THP-1 (ATCC TIB-202), hPSC-CMs (iCell Cardiomyocytes, Cellular Dynamics), and TF-1 (ATCC CRL-2003) were cultured according to the manufacturer's protocol. TF-1 cells were cultured in RPMI media with 10% FBS supplemented with 2 ng/ml recombinant human GM-CSF (Biotechne 7954-GM). TF-1 cells were starved in RPMI media with 10% FBS but no GM-CSF for 24 h before any experiment. iCell Cardiomyocytes IPSC donor 01434 were used for all experiments. Briefly, hPSC-derived CMs were plated on 0.1% gelatin-coated 6 well plates in iCell Cardiomyocyte Plating Medium (CDI) at a density of $3-4 \times 10^5$ cells per well and incubated at 37 °C in 5% CO_2 for 4 days. Two days after plating, the plating medium was replaced with iCell cardiomyocyte maintenance medium (CDI). After 4 days of monolayer preculture, cardiomyocytes were lifted using trypLE Express (Gibco Life Technologies) and prepared for organoid fabrication. Human cardiac ventricular FBs (CC-2904, 0000401462, Lonza) were cultured in FGM-3 medium (Lonza), at passages 3–4 for organoid fabrication. HUVECS (C2519A) were cultured in EGM-2 medium (Lonza) and were used in passages 2–3 for organoid fabrication. Human adipose-derived stem cells (hADSCs; PT-5006, 0000410257, Lonza) were cultured in low-glucose Dulbecco's modified Eagle's medium supplemented with 10% FBS and 1% Penicillin-streptomycin, 1% glutamine, and 1% antimycin (Gibco Life Technologies). hADSCs were used in passages 3–5 for organoid fabrication[34].

Fabrication of organoids

We have previously described the fabrication of our organoids[34,35]. Briefly, agarose molds were used as molds for microtissue fabrication from commercial master micromolds from Microtissues, with each mold containing a 7×5 matrix of recesses. Organoid cellular suspensions are composed of 55% hPSC–CMs, 24% hcFBs, 14% HUVECs, and 7% hADSCs in the medium at a concentration of 2×10^6 cells/ml. To generate organoids with a diameter -150 mm, 75 ml of the organoid suspension was added into the molds and allowed to settle for 15 min. Upon settling, 2 ml of medium was added to submerge the molds in a 12-well plate. Media was changed every 2 days for the entirety of the experiment. The organoids were allowed to form for 4 days, with D4 of the assembly being denoted as D0 of the experiment. IL-1b treatment protocol was then initiated for 4 days. Organoid media is composed of a ratiometric combination of cell-specific medium reflecting the starting cell ratio of the organoid. The CM-specific component was defined as a glucose-containing F12/DMEM medium with 10% FBS, 1% glutamine, and 1% non-essential amino acids (Gibco).

Contraction analysis for FAC

Videos of spontaneously beating organoids from each group were recorded 10 min after removing the 12-well plates from the incubator. This was done to equilibrate plates at room temperature and reduce variation in temperature-mediated changes in the beating. Recording of the videos was performed with a Carl Zeiss Axiovert a1 Inverted Microscope and Zen 2011 software (Zeiss). Threshold edge-detecting in ImageJ software (US National Institutes of Health NIH)) was used on high-contrast organoid picture series and graphed over the number of frames. Each beating profile was used to calculate the FAC amplitude (fractional change in the area of the organoid at maximum contraction and relaxation).

Fluorescence imaging and analysis

Organoids were harvested and flash frozen in Tissue-Tek Optimal Cutting Temperature (OCT) compound (Sakura). Embedded organoids were cryosectioned (7 mm thick) onto glass slides for immunofluorescence staining. Section fixation took place in precooled acetone (−20 °C for 12 min). After two washes in phosphate buffer saline (PBS) with 0.1% Triton X-100 (Sigma) (PBST), a blocking buffer was made with 10% serum corresponding to the host species of the secondary antibodies in PBST. Blocking buffer was added to sections for 1 h at room temperature. The sections were then washed two times (5 min) with PBST and stained for primary antibody at 1:200 in PBST for 1 h at room temperature: rabbit anti-alpha sarcomeric actinin (ab90776, Lot: GR239387-31, Abcam), mouse anti-vimentin (ab8069, Lot: GR3379996-2, Abcam). Sections were then washed two times (5 min) with PBST and stained with complementary secondary antibody diluted in PBST (1:200) for 1 h at room temperature: goat anti-rabbit Alexa Fluor 647 (ab150083, GR3415075-1, Abcam, 1:1000), goat anti-mouse Alexa Fluor 488 (ab150113, Lot: 1001008179, Abcam, 1:1000). After washing with PBST two times (5 min), nuclei were stained with NucBlue (R37606, Lot: 2165134, Invitrogen) diluted in PBST for 20 min at room temperature. Sections were then washed three times (3 min) in PBST, and coverslips were added using Fluoroshield (Lot: MKCG4762, Sigma) and stored at 4 °C until imaging. A TCS SP5 AOBS laser-scanning confocal microscope (Leica Microsystems) was used to image microtissue sections for which z-stacks with a thickness of 3–4 mm and a step size of 1 mm were used. Intensities for alpha sarcomeric actinin and vimentin were calculated using ImageJ Threshold Detection after splitting images into individual channels. The threshold area was then measured and normalized to the cross-sectional area of each organoid being measured in the image.

Mini-binder evaluation on hCOs

Mini-binders were added to organoids concurrently with IL-1b on Days 2 and 4 upon media replacement: ILR80mb and ILR81mb were each added to the organoid culture to achieve a final concentration of 1 uM. Briefly, IL-1b (Cat:4128-10, Lot: P1098, Biovision) was added to the organoid culture on days 0 and 2 upon media replacement at 1 ng/ml. IL-1b was reconstituted at the recommended stock concentration (with recommended solvents) concentration per the manufacturer's instructions[26].

Eve tech cytokine plexing

Supernatants were collected from organoid culture on day 4 and were analyzed for cytokine levels using a Human Cytokine Array Proinflammatory Focused 15 plex (Eve Technologies, Calgary, AB).

Statistical analysis

Differences between experimental groups were analyzed using Microsoft Excel (v13.7) and GraphPad Prism (v9.1.1) statistical tools. Sample distribution was assumed normal with equal variance. Statistical analysis was performed using Student's t-tests or one-way ANOVA with post-hoc Bonferroni-corrected t-tests and $P < 0.05$ was considered to be statistically significant. Sample sizes of biologically independent samples per group and the number of independent experiments are indicated in figure legends

Reporting summary

Further information on research design is available in the Nature Portfolio Reporting Summary linked to this article.

Data availability

The source data included in this manuscript is available in the Source data file attached to this manuscript. Full raw data and DNA sequencing data are available on zenodo.org (accession code: 12797779) [https://doi.org/10.5281/zenodo.12797779]. The final sequences of the designed inhibitors included in this manuscript are provided in Supplementary Table 2. Structures used in this study are publicly available under accession codes 1N26 [https://doi.org/10.2210/pdb1N26/pdb], 1P9M [https://doi.org/10.2210/pdb1P9M/pdb], and 1IRA [https://doi.org/10.2210/pdb1IRA/pdb]. Crystal structures obtained in this study were deposited into the Protein Data Bank under accession code: 8UPB [https://doi.org/10.2210/pdb8UPB/pdb] (IL-6Rmb), 8UPA [https://doi.org/10.2210/pdb8UPA/pdb] (GP130mb-GP130 complex), and 8UOS [https://doi.org/10.2210/pdb8UOS/pdb] (IL-1Rmb). Source data are provided in this paper.

Code availability

The scripts and codes used in this manuscript are available at zenodo.org (accession code: 12797779 [https://doi.org/10.5281/zenodo.12797779]). The Rosetta modeling suite (https://www.rosettacommons.org) is available to academic and non-commercial users for free. Commercial licenses for the suite are also available through the University of Washington Technology Transfer Office. The source code for RIF docking is available at https://github.com/rifdock/rifdock. FACS was collected in Sony SH800 software suites. Flow cytometry for mammalian cells was collected in Thermo Attune NxT flow cytometer software suites. Binding data was collected in Octet RED96 and processed using Octet Analysis software. Fluorescence plate reading was collected in BioTek Synergy Neo2 Reader. Data was analyzed and plotted using python3.6 with seaborn0.12.1, matplotlib3.6.1, and GraphPad Prism9. Flow cytometry data was processed by Flowjo v9. The figures were generated by Adobe Illustrator software 2023.

References

1. Fajgenbaum, D. C. & June, C. H. Cytokine storm. *N. Engl. J. Med.* **383**, 2255–2273 (2020).
2. Gu, Y. et al. The mechanism behind influenza virus cytokine storm. *Viruses* **13**, 1362 (2021).
3. Yang, L. et al. The signal pathways and treatment of cytokine storm in COVID-19. *Signal Transduct. Target. Ther.* **6**, 255 (2021).
4. Velazquez-Salinas, L., Verdugo-Rodriguez, A., Rodriguez, L. L. & Borca, M. V. The role of interleukin 6 during viral infections. *Front. Microbiol.* **10**, 1057 (2019).
5. Galván-Román, J. M. et al. IL-6 serum levels predict severity and response to tocilizumab in COVID-19: an observational study. *J. Allergy Clin. Immunol.* **147**, 72–80.e8 (2021).
6. Mudd, P. A. et al. Distinct inflammatory profiles distinguish COVID-19 from influenza with limited contributions from cytokine storm. *Sci. Adv.* **6**, eabe3024 (2020).
7. Moore, J. B. & June, C. H. Cytokine release syndrome in severe COVID-19. *Science* **368**, 473–474 (2020).
8. Thompson, B. T., Chambers, R. C. & Liu, K. D. Acute respiratory distress syndrome. *N. Engl. J. Med.* **377**, 562–572 (2017).
9. de Jong, M. D. et al. Fatal outcome of human influenza A (H5N1) is associated with high viral load and hypercytokinemia. *Nat. Med.* **12**, 1203–1207 (2006).
10. REMAP-CAP Investigators et al. Interleukin-6 receptor antagonists in critically Ill patients with Covid-19. *N. Engl. J. Med.* **384**, 1491–1502 (2021).
11. Rosas, I. O. et al. Tocilizumab in hospitalized patients with severe covid-19 pneumonia. *N. Engl. J. Med.* **384**, 1503–1516 (2021).
12. Salama, C. et al. Tocilizumab in patients hospitalized with covid-19 pneumonia. *N. Engl. J. Med.* **384**, 20–30 (2021).
13. Sinha, P. et al. Prevalence of phenotypes of acute respiratory distress syndrome in critically ill patients with COVID-19: a prospective observational study. *Lancet Respir. Med.* **8**, 1209–1218 (2020).
14. Cao, L. et al. Design of protein binding proteins from target structure alone. *Nature.* https://doi.org/10.1038/s41586-022-04654-9 (2022).
15. Hunt, A. C. et al. Multivalent designed proteins neutralize SARS-CoV-2 variants of concern and confer protection against infection in mice. *Sci. Transl. Med.* **14**, eabn1252 (2022).
16. Boulanger, M. J., Chow, D., Brevnova, E. E. & Garcia, K. C. Hexameric structure and assembly of the interleukin-6/IL-6 α-receptor/gp130 complex. *Science* **300**, 2101–2104 (2003).
17. Thomas, C., Bazan, J. F. & Garcia, K. C. Structure of the activating IL-1 receptor signaling complex. *Nat. Struct. Mol. Biol.* **19**, 455–457 (2012).
18. Varghese, J. N. et al. Structure of the extracellular domains of the human interleukin-6 receptor α-chain. *Proc. Natl. Acad. Sci.* **99**, 15959–15964 (2002).
19. Schreuder, H. et al. A new cytokine-receptor binding mode revealed by the crystal structure of the IL-1 receptor with an antagonist. *Nature* **386**, 194–200 (1997).
20. Dou, J. et al. De novo design of a fluorescence-activating β-barrel. *Nature* **561**, 485–491 (2018).
21. Schneidman-Duhovny, D., Inbar, Y., Nussinov, R. & Wolfson, H. J. PatchDock and SymmDock: servers for rigid and symmetric docking. *Nucleic Acids Res.* **33**, W363–W367 (2005).
22. Silva, D.-A. et al. De novo design of potent and selective mimics of IL-2 and IL-15. *Nature* **565**, 186–191 (2019).
23. Rocklin, G. J. et al. Global analysis of protein folding using massively parallel design, synthesis, and testing. *Science* **357**, 168–175 (2017).
24. Rose-John, S., Jenkins, B. J., Garbers, C., Moll, J. M. & Scheller, J. Targeting IL-6 trans-signalling: past, present and future prospects. *Nat. Rev. Immunol.* **23**, 666–681 (2023).
25. Fourcin, M. et al. Involvement of gp130/interleukin-6 receptor transducing component in interleukin-11 receptor. *Eur. J. Immunol.* **24**, 277–280 (1994).
26. Arhontoulis, D. C. et al. Human cardiac organoids to model COVID-19 cytokine storm induced cardiac injuries. *J. Tissue Eng. Regen. Med.* **16**, 799–811 (2022).
27. Cao, L. et al. De novo design of picomolar SARS-CoV-2 miniprotein inhibitors. *Science* **370**, 426–431 (2020).
28. Studier, F. W. Protein production by auto-induction in high-density shaking cultures. *Protein Expr. Purif.* **41**, 207–234 (2005).
29. Kabsch, W. XDS. *Acta Crystallogr. D. Biol. Crystallogr.* **66**, 125–132 (2010).
30. McCoy, A. J. et al. Phaser crystallographic software. *J. Appl. Crystallogr.* **40**, 658–674 (2007).
31. Emsley, P., Lohkamp, B., Scott, W. G. & Cowtan, K. Features and development of *Coot*. *Acta Crystallogr. D. Biol. Crystallogr.* **66**, 486–501 (2010).
32. Liebschner, D. et al. Macromolecular structure determination using X-rays, neutrons and electrons: recent developments in Phenix. *Acta Crystallogr. Sect. Struct. Biol.* **75**, 861–877 (2019).
33. Battye, T. G. G., Kontogiannis, L., Johnson, O., Powell, H. R. & Leslie, A. G. W. iMOSFLM: a new graphical interface for diffraction-image processing with MOSFLM. *Acta Crystallogr. D. Biol. Crystallogr.* **67**, 271–281 (2011).
34. Richards, D. J. et al. Inspiration from heart development: biomimetic development of functional human cardiac organoids. *Biomaterials* **142**, 112–123 (2017).
35. Richards, D. J. et al. Human cardiac organoids for the modelling of myocardial infarction and drug cardiotoxicity. *Nat. Biomed. Eng.* **4**, 446–462 (2020).

Author contributions

B.H., B.C., M.T.B., D.C.A., and M.E. contributed equally to this study. B.H., B.C., and D.B. designed the research. D.B., K.C.G., L.S., Y.M., and D.F. supervised the research. B.H. and B.C. designed and optimized all the minibinders. B.H. screened and characterized all the binders. L.C., M.D., and S.C. produced the minibinders with low endotoxin protocol. M.T.B. solved IL-6Rmb and GP130mb crystal structure. K.J. solved the IL-1Rmb crystal structure. M.T.B. and K.J. produced the GP130 and IL-1R1 target proteins. D.C.A. and N.H. conducted the organoid experiments and characterized the designed antagonists using the organoid model. M.T.B, M.E., M. Abedi, H.T., and M. Ahlrichs conducted the IL-6-related cell signaling assay, proliferation assay, and cell culture. M. Abedi performed the SPR crossreactivity binding experiment. B.H. conducted the IL-1-related cell signaling assay. S.F.H., A.A., C.C., I.G., and B.H. performed the yeast display and NGS experiment for all minibinders. B.H. and D.B. wrote the manuscript with input from the other authors. All authors analyzed data and revised the manuscript.

Competing interests

B.H., B.C., M. Abedi., L.C., L.S., and D.B. at the University of Washington are co-inventors on the provisional patent application MBHB 23-1545-US-PRO (submitted) that incorporates the discoveries of IL-6R/IL1R/GP130 minibinders described in this manuscript. The remaining authors declare no competing interests.

Additional information

Supplementary information The online version contains supplementary material available at https://doi.org/10.1038/s41467-024-50919-4.

Correspondence and requests for materials should be addressed to David Baker.

Peer review information *Nature Communications* thanks Bert Janssen and the other, anonymous, reviewers for their contribution to the peer review of this work. A peer review file is available.

Reprints and permissions information is available at http://www.nature.com/reprints

Publisher's note Springer Nature remains neutral with regard to jurisdictional claims in published maps and institutional affiliations.